Supporting Information

Dual-Stage K-ion Intercalation in V$_2$O$_5$-Conductive Polymer Composite

Daniel S. Charles,[†] Fenghua Guo,[†] Xiaoqiang Shan,[†] SaeWon Kim,[†] Zachary W. Lebens-Higgins,[€] Wenqian Xu,[§] Dong Su,[⊥,θ] Louis F. J. Piper,[€] Xiaowei Teng[†]*

[†]Department of Chemical Engineering, University of New Hampshire, Durham, New Hampshire 03824, USA

[€] Department of Physics, Applied Physics and Astronomy, Binghamton University, Binghamton, New York 13902, USA

[§] X-ray Science Division, Advanced Photon Source, Argonne National Laboratory, Lemont, Illinois 60439, USA

[⊥] Center for Functional Nanomaterials, Brookhaven National Laboratory, Upton, New York 11973, USA

[θ] Institute of Physics, Chinese Academy of Sciences, Beijing, 100190, China
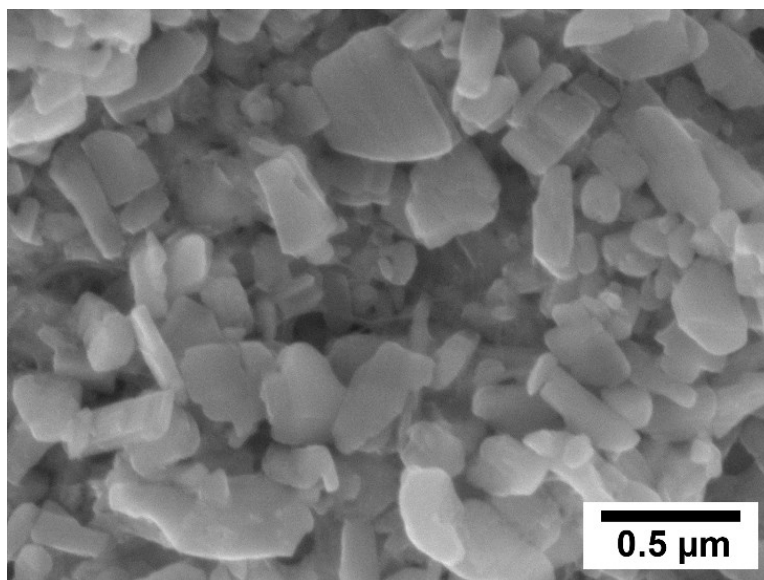

*Corresponding email: xw.teng@unh.edu

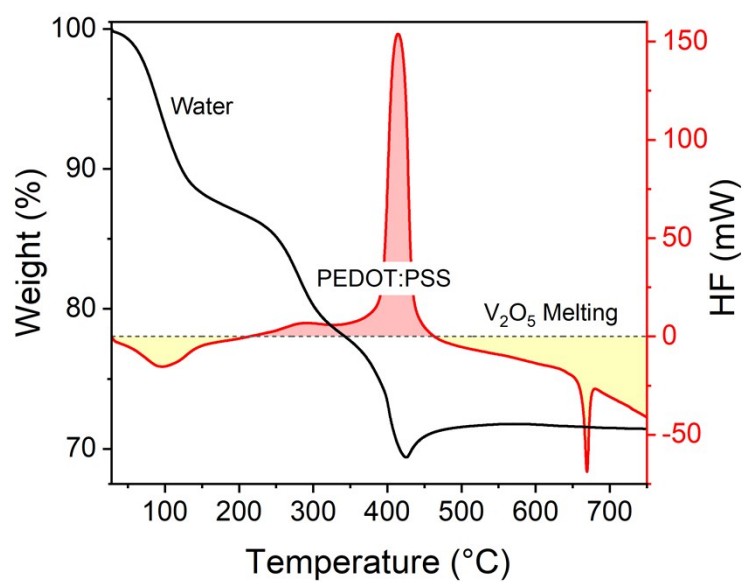**Figure S1.** Scanning electron microscopy image of commercial bulk V_2O_5 showing the particle morphology.

Figure S2. Thermogravementric Analysis and Differential Scanning Calorimetry of VPP measured in air at heating rate of 10°C min^{-1}.
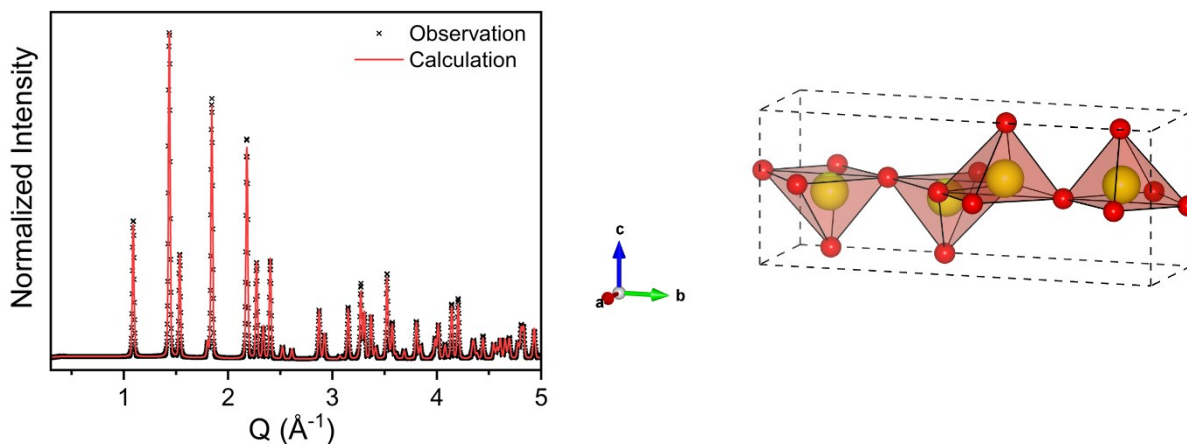
Figure S3. Synchrotron X-ray diffraction of commercial bulk V_2O_5, which confirmed the α-V_2O_5 possessing an orthorhombic structure with Pmmn symmetry with lattice parameters of a=11.5216 Å, b=3.5669 Å, and c= 4.3750 Å and a goodness of fit Rw = 6.165%. Atom Positions are provide in **Table S2**.
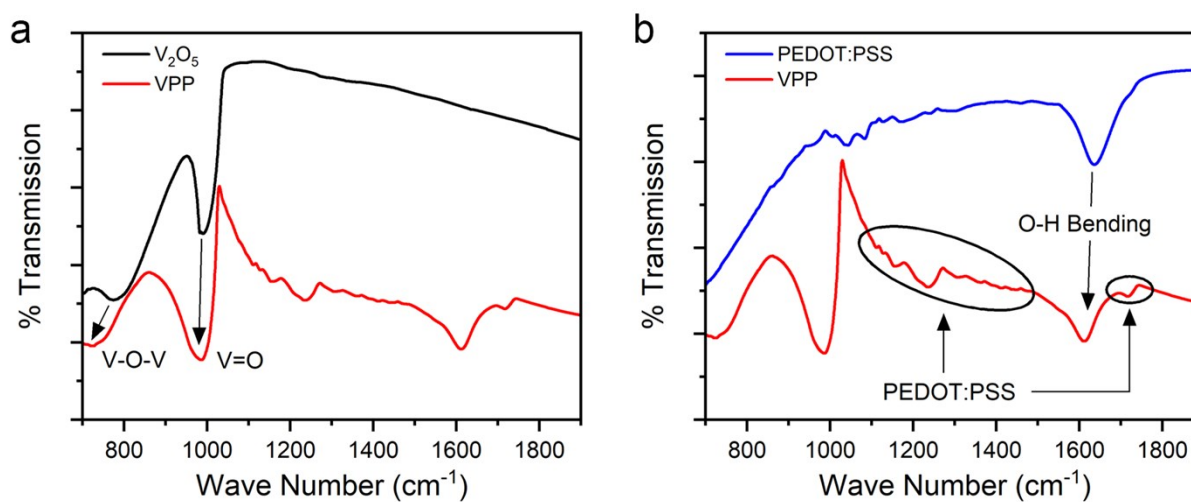

Figure S4. FTIR spectra of (a) VPP powder and V_2O_5 precursor materials, (b) VPP powder and 3-4 % PEDOT: PSS conductive polymer in H_2O.
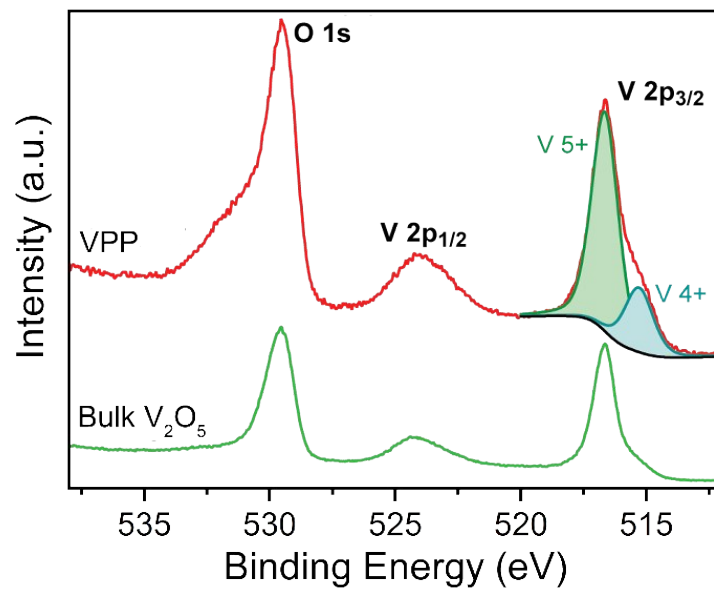
Figure S5. X-ray Photoelectron Spectroscopy of the V2p - O1s region of VPP showing the increased portion of V^{4+}, consistent with the systematic oxygen vacancies associated with the intercalative bilayer structure.
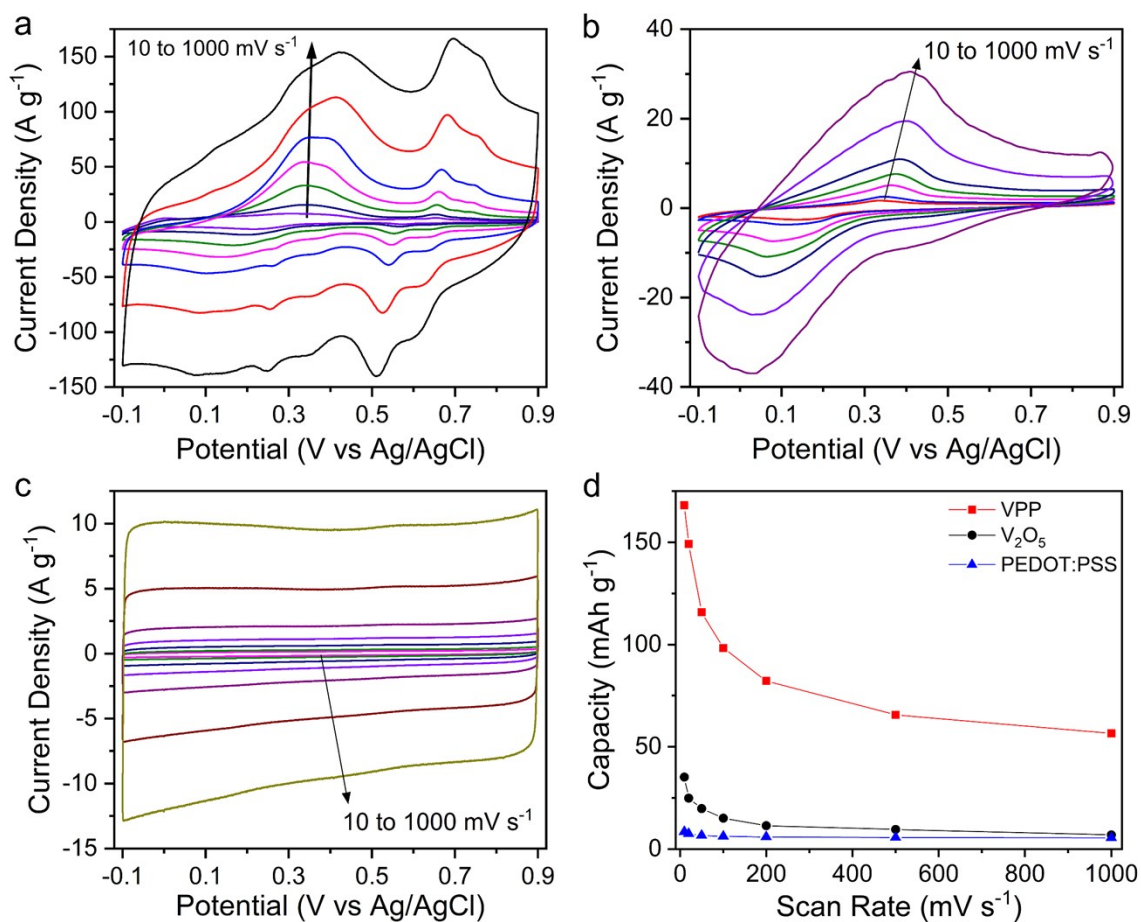
Figure S6. Cyclic Voltammetry measurements of (a) VPP in a three-electrode half-cell, (b) commercial bulk V_2O_5, and (c) PEDOT: PSS in a 1 M KCl electrolyte and -0.1 to 0.9 V vs. Ag/AgCl potential window at various scan rates from 10 to 1000 mV s^{-1}. (d) The calculated total capacities (both charging and discharging) of VPP, in comparison with those of commercial bulk V_2O_5 and PEDOT: PSS.
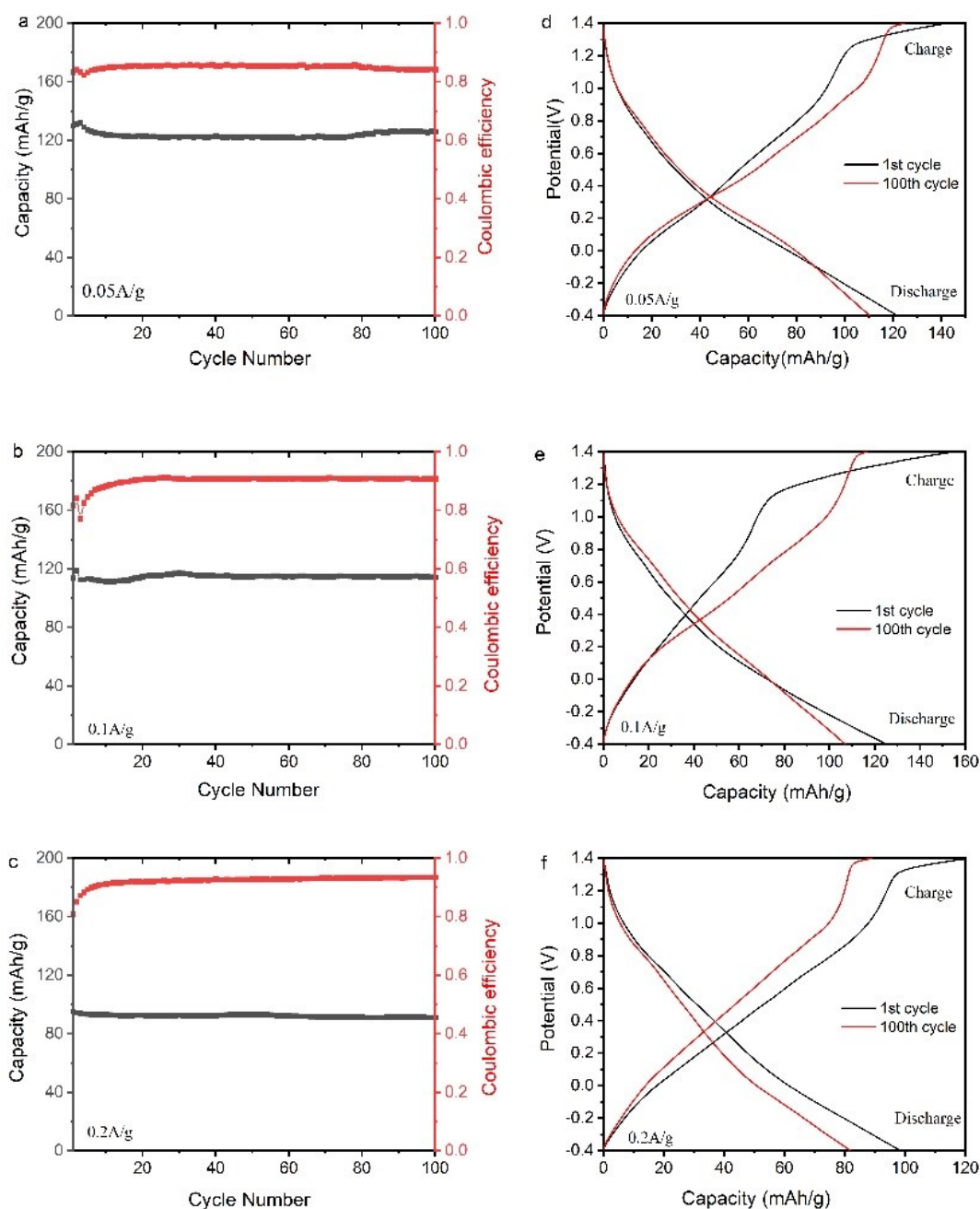
Figure S7. Long-term cycling of VPP in a two-electrode full-cell. (a, b, c) discharge capacities and Coulombic efficiencies as a function of cycling number at current densities of 0.05, 0.1, and 0.2 A g^{-1} after 100 cycles; (d, e, f) CPs at the 1st and 100th cycles at current densities of 0.05, 0.1, and 0.2 A g^{-1}. Notes: The two-electrode cells for VPP measurement include the cathode (0.4 mg VPP mixed with 1.6 mg carbon black) and the anode (20mg XC-72 active carbon) under the potential window between -0.4V and 1.4V in a 3M KCl electrolyte. As shown in the following Figure S7, the anode capacity is much higher than the cathode capacity (and VPP capacity in the cathode is also much higher than carbon black capacity in the cathode); therefore, the overall cell capacity is limited by the VPP electrode.
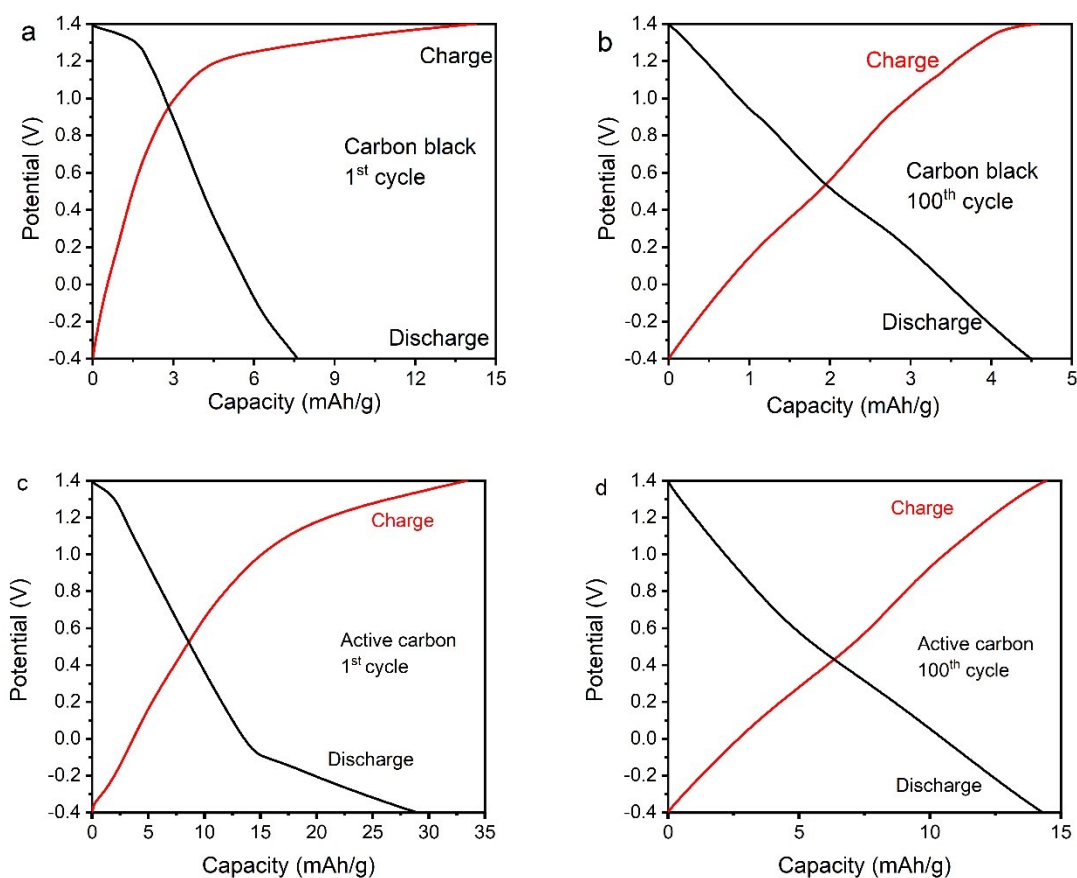
Figure S8. CP curves of conducting carbon including (a, b) graphitic carbon black and (c,d) high-surface-area active carbon (XC-72) measured in a two-electrode full-cell at a current density of 0.05 g^{-1} at the (a, c) 1st cycles and (b, d) 100th cycles. Comparing to the discharge capacity of VPP at the same current density (126 mAh/g, Figure S6a), the capacity contribution from conducting carbon is negligible. Notes: The two-electrode cells for carbon black measurement include the cathode (2mg carbon black) and the anode (20mg XC-72 active carbon) under the potential window between -0.4V and 1.4V in a 3M KCl electrolyte; The two-electrode cells for XC-72 active carbon measurement include the cathode (2mg XC-72 active carbon) and the anode (20mg XC-72 active carbon) under the potential window between -0.4V and 1.4V in a 3M KCl electrolyte.
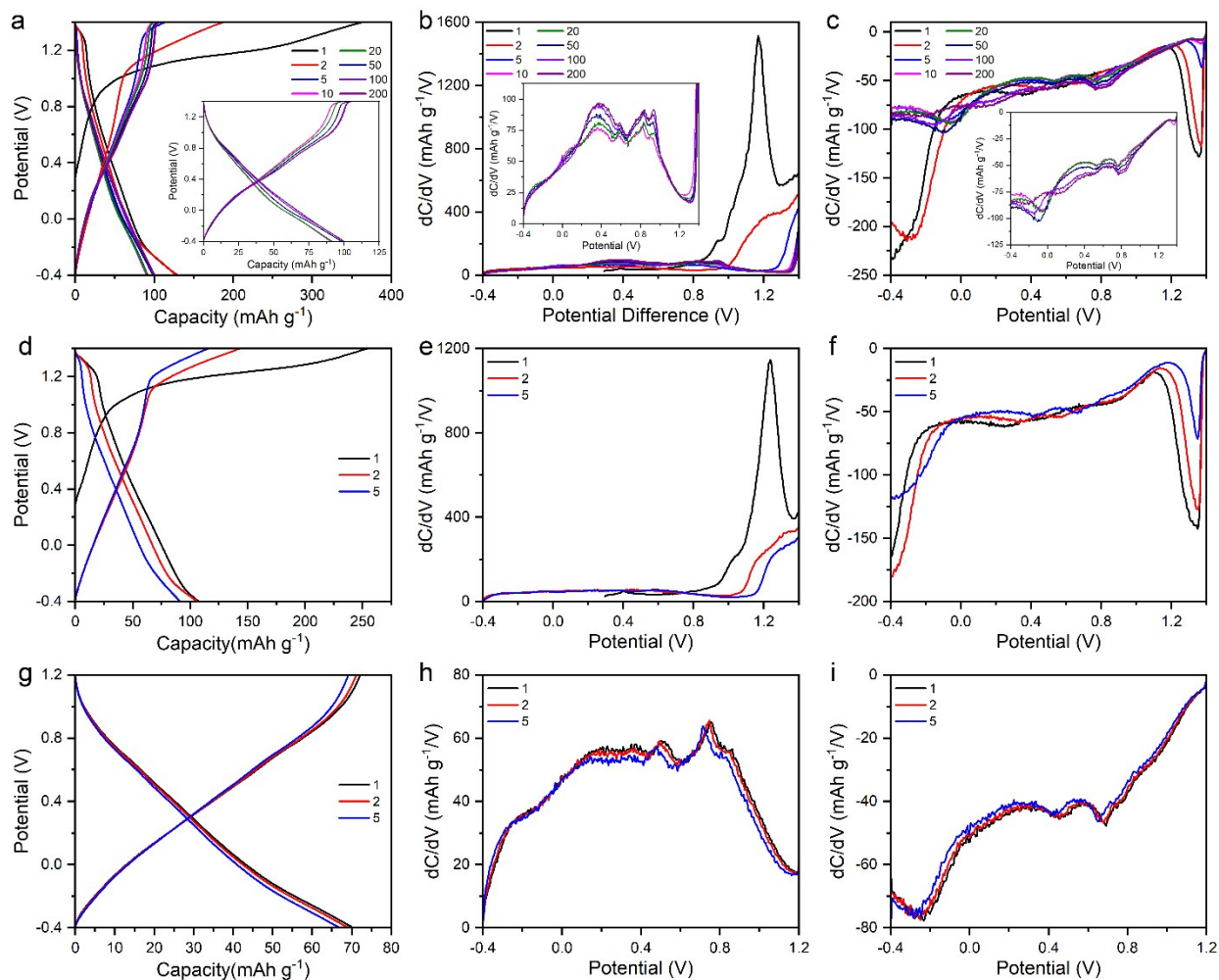
Figure S9. (a) Charge-discharge curves of VPP full-cell cycled at 0.2 A g^{-1} in a 1.8 V potential window and the corresponding dC/dV curves for the (b) charging and (c) discharging segments. (d) Charge-discharge curves for VPP full-cells startup process cycled at 2 A g^{-1} in a 1.8 V potential window, and the corresponding dC/dV curves for the (e) charging and (f) discharging segments. (g) Charge-discharge curves of VPP full-cell cycled at 2 A g^{-1} in the reduced 1.6 V potential window following the startup process and the corresponding dC/dV curves for the (h) charging and (i) discharging segments.
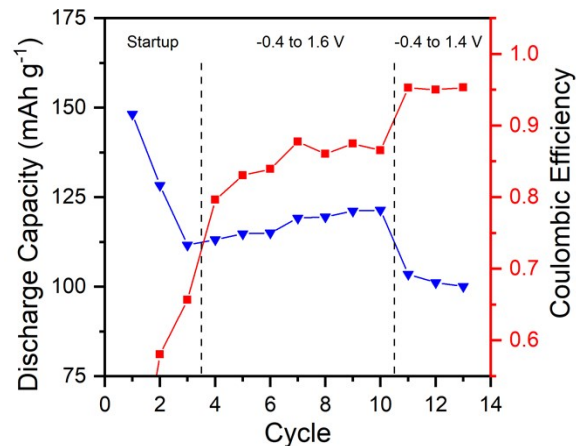
Figure S10. Discharge capacity and coulombic efficiency upon the reduction of the full-cell potential window from -0.4 to 1.6 V to -0.4 to 1.4 V at a current density of 0.1 A g^{-1}.
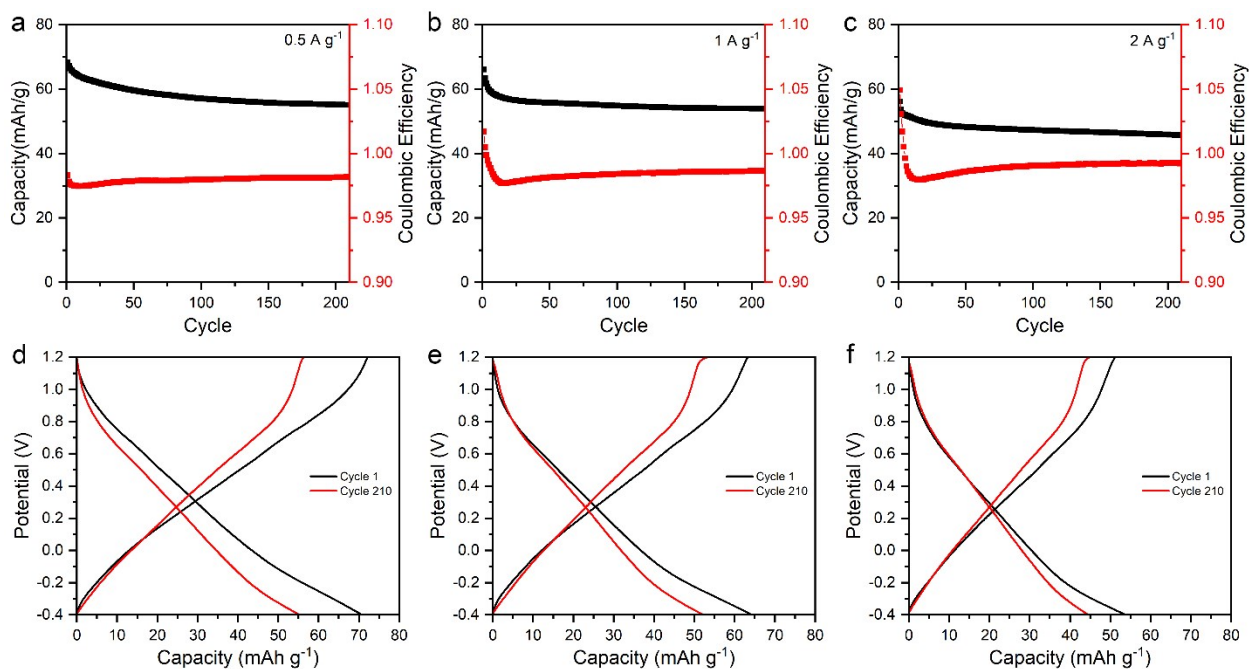

Figure S11. Measured discharge capacities from cycling of VPP in asymmetric full-cells at 1.2V at (a) 0.5, (b) 1.0, and (c) 2.0 A g^{-1}. The corresponding charge-discharge curves at the first and last cycle at current densities of (d) 0.5, (e) 1.0, and (f) 2.0 A g^{-1}.
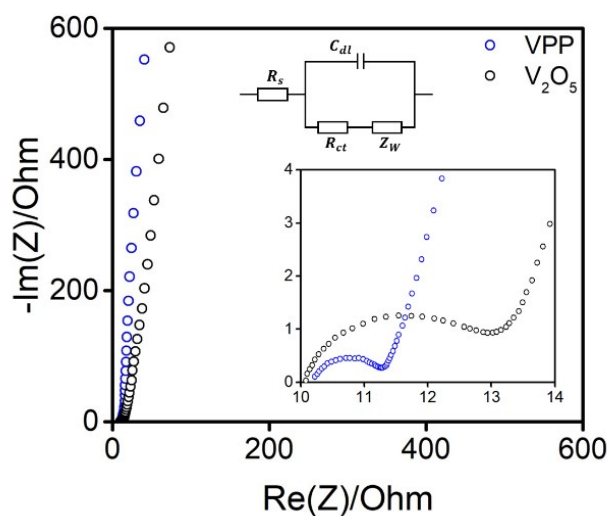
Figure S12. Nyquist Plot of the electrochemical impedance of VPP and V_2O_5.
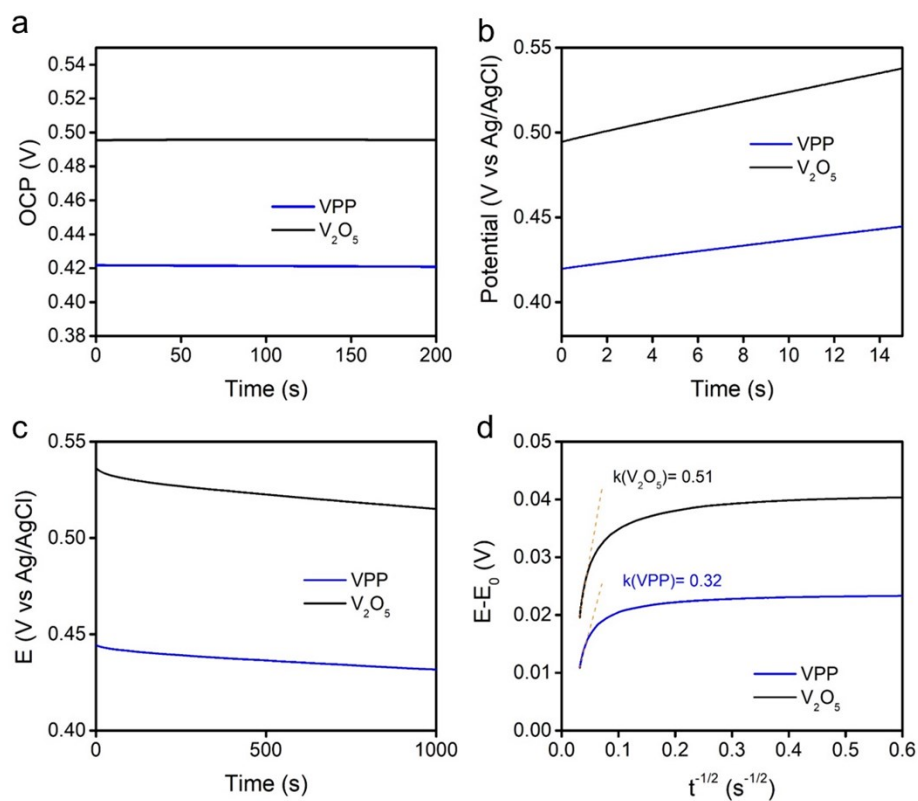

Figure S13. Diffusivity measurements of VPP and V_2O_5 with (a) Open circuit voltages before constant current pulse; (b) CP test with charge current pulse; (c) relaxation curves; and (d) slopes for diffusivity calculation.
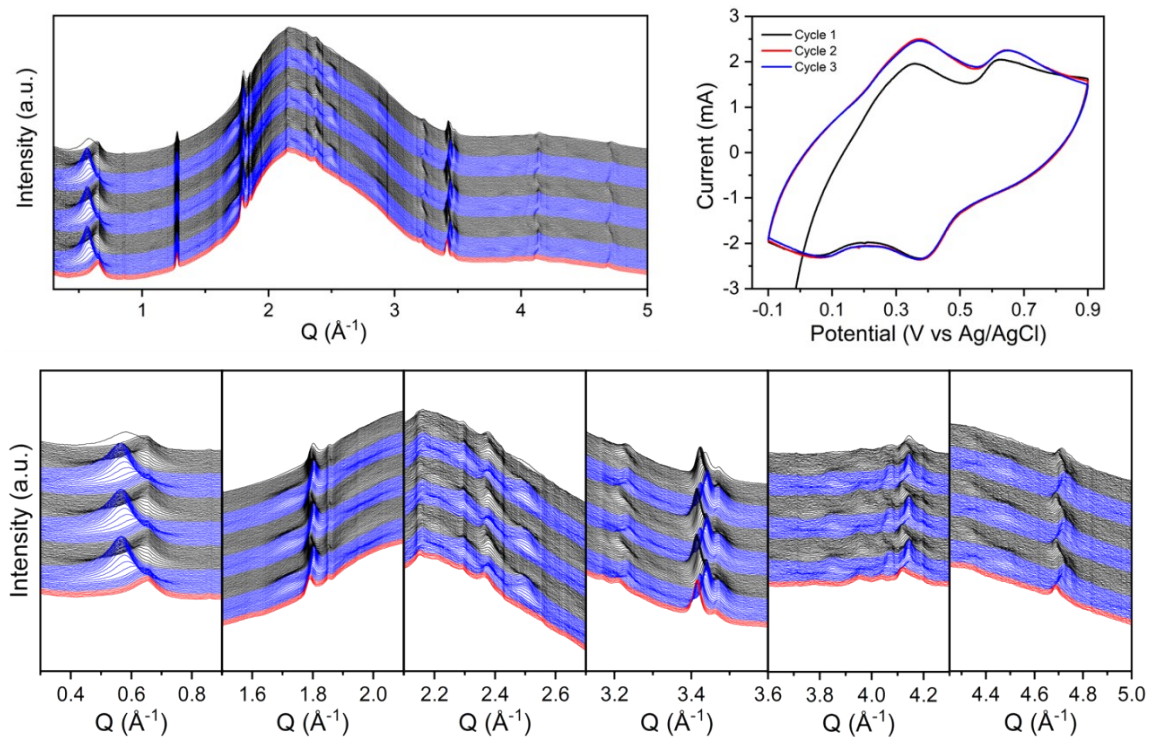
Figure S14. (a) Full *in situ* X-ray diffraction scans of VPP during electrochemical cycling at 1 mV s^{-1} within a 1 V potential window (-0.1 V to 0.9 V vs. Ag/AgCl) in 3 M KCl electrolyte and (b) the associated CV collected during the *in situ* measurement. (c) Zoomed in sections of the in situ XRD scans showing the evolution of various peaks during cycling.
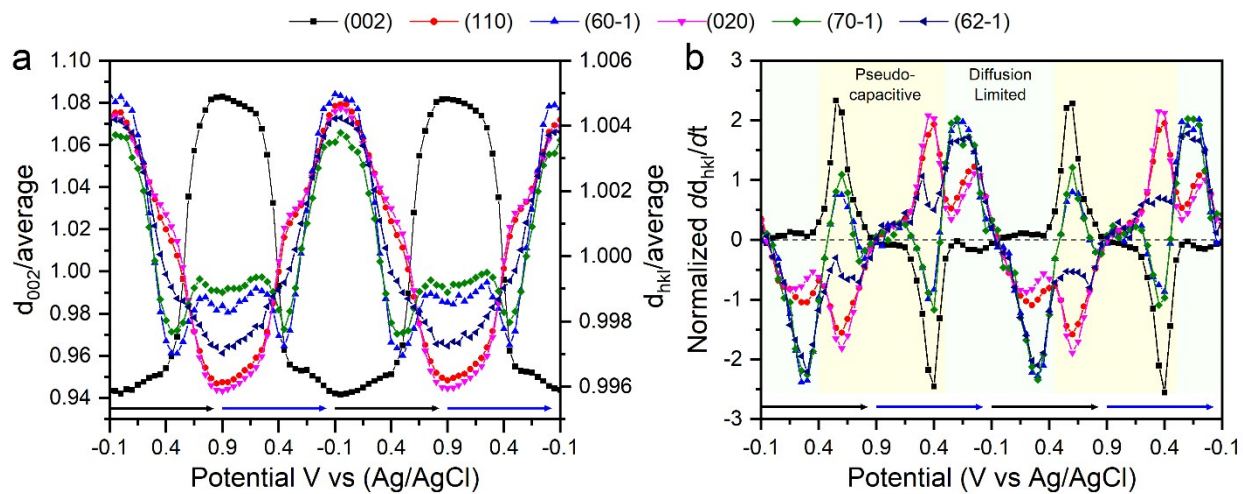
Figure S15. In situ XRD peak evolution of VPP at 1 mV s^{-1} in a 1.0 V potential window.
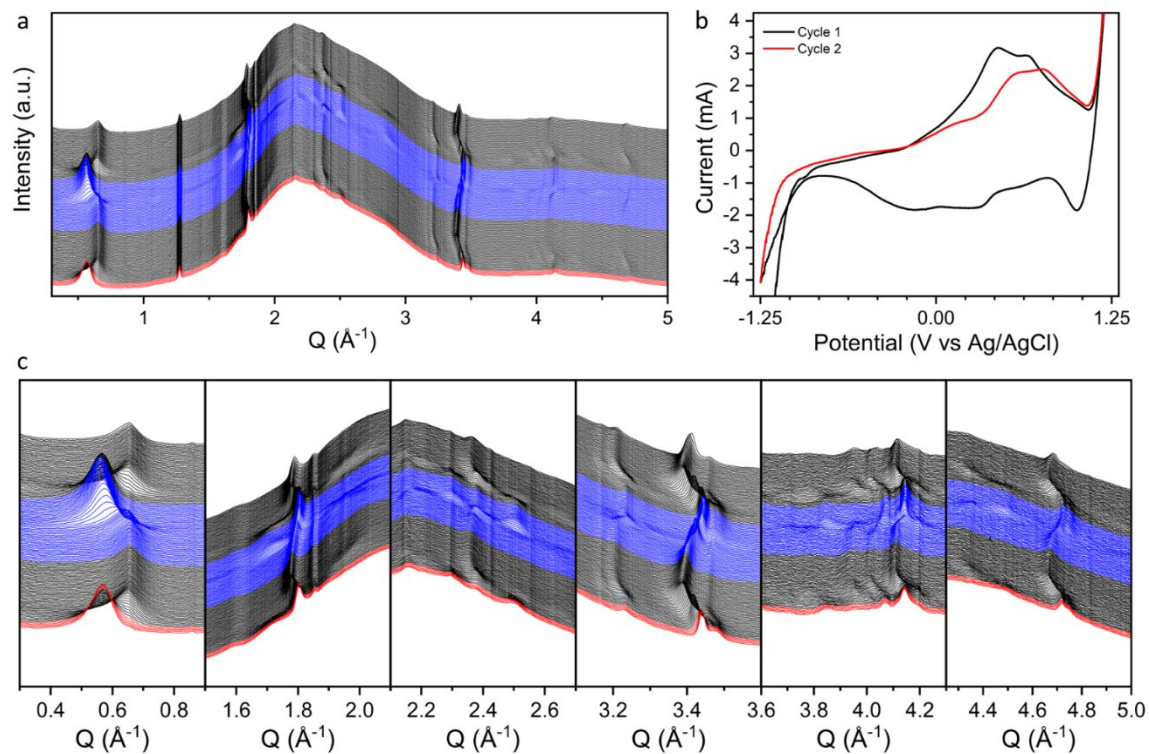
Figure S16. *In situ* X-ray Diffraction of VPP during electrochemical cycling at 1 mV s^{-1} in a 2.5 V potential window (-1.25 to 1.25 V vs. Ag/AgCl) in 3 M KCl electrolyte.
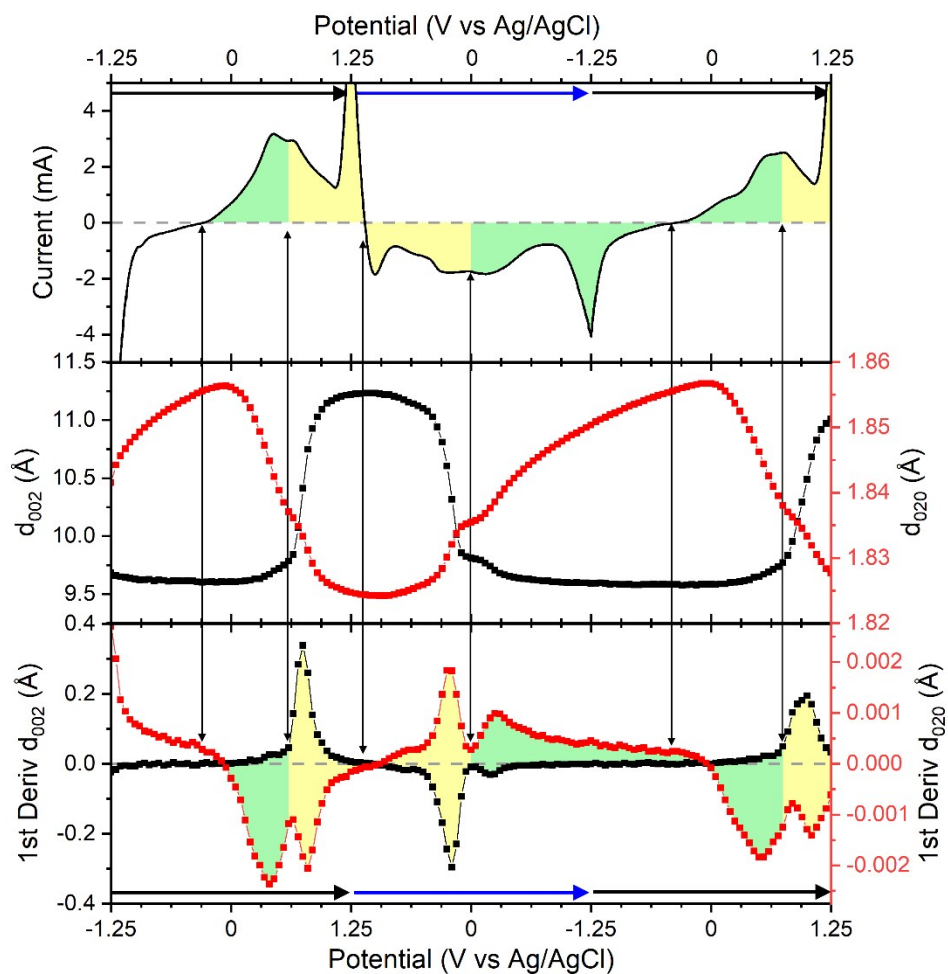
Figure S17. In situ X-ray Diffraction peak evolution of the (002) and (020) diffraction planes of VPP during electrochemical cycling in a 2.5 V potential (-1.25 to 1.25 V vs. Ag/AgCl).
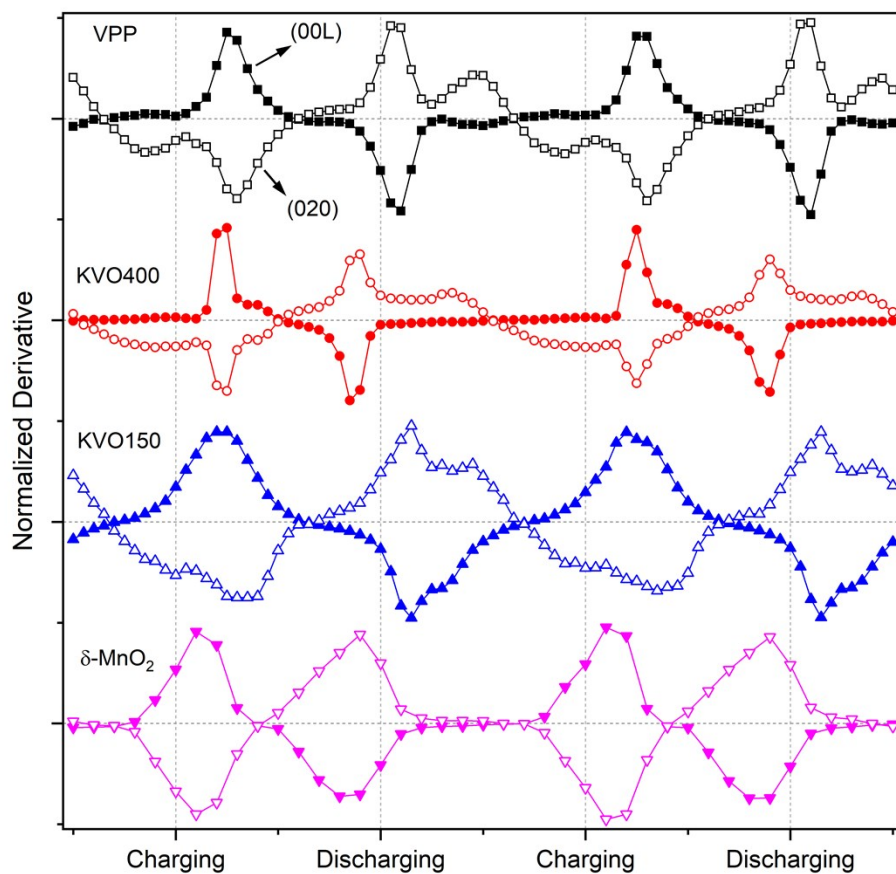
Figure S18. Comparisons of the peak evolution for the (002) and (020) during the electrochemical cycling for VPP, crystalline $K_{0.33}V_2O_5$, disordered layered $K_{0.22}V_2O_5 \cdot 0.8H_2O$, and sodium birnessite δ-$Na_{0.27}MnO_2 \cdot 6H_2O$ layered materials.

Table S1. Comparison of characteristics of various bi-layered vanadium oxide materials (δ-$A_xV_2O_5 \cdot nH_2O$).

	V$_2$O$_5$/PEDOT: PSS intercalative materials (VPP)	hydrated disordered potassium vanadium oxide materials (KVO)
Synthesis	Dissolution & recrystallization	Co-precipitation
	A top-down approach	A bottom-up approach
Crystallinity	ordered	disordered
Morphology	1D nanoribbon	2D nanosheet
Interlayer Distance	2.20 nm	1.09 nm
Interlayer Species	Water, K-ion, and PEDOT:PSS	Water, K-ion

Table S2. Refined atom positions for the commercial bulk V$_2$O$_5$ (Figure S3).

Atom	x	y	z	Occupancy	Uiso
V1	0.25000	0.10110(6)	0.39189(12)	1.000	0.00804(16)
O1	0.25000	0.10409(20)	0.0322(4)	1.000	0.0160(6)
O2	0.25000	0.56897(16)	0.5045(4)	1.000	0.0053(7)
O3	0.25000	0.25000	0.5025(6)	1.000	0.0110(10)